

VIP **Single-Atom Catalysts** Very Important PaperDeutsche Ausgabe: DOI: 10.1002/ange.201905241
Internationale Ausgabe: DOI: 10.1002/anie.201905241

A Single-Atom Iridium Heterogeneous Catalyst in Oxygen Reduction Reaction

Meiling Xiao⁺, Jianbing Zhu⁺, Gaoran Li, Na Li, Shuang Li, Zachary Paul Cano, Lu Ma, Peixin Cui, Pan Xu, Gaopeng Jiang, Huile Jin, Shun Wang,* Tianpin Wu,* Jun Lu, Aiping Yu, Dong Su* und Zhongwei Chen*

Abstract: Combining the advantages of homogeneous and heterogeneous catalysts, single-atom catalysts (SACs) are bringing new opportunities to revolutionize ORR catalysis in terms of cost, activity and durability. However, the lack of high-performance SACs as well as the fundamental understanding of their unique catalytic mechanisms call for serious advances in this field. Herein, for the first time, we develop an Ir-N-C single-atom catalyst (Ir-SAC) which mimics homogeneous iridium porphyrins for high-efficiency ORR catalysis. In accordance with theoretical predictions, the as-developed Ir-SAC exhibits orders of magnitude higher ORR activity than iridium nanoparticles with a record-high turnover frequency (TOF) of $24.3 e^- \text{ site}^{-1} \text{ s}^{-1}$ at 0.85 V vs. RHE) and an impressive mass activity of $12.2 \text{ A mg}^{-1}_{\text{Ir}}$, which far outperforms the previously reported SACs and commercial Pt/C. Atomic structural characterizations and density functional theory calculations reveal that the high activity of Ir-SAC is attributed to the moderate adsorption energy of reaction intermediates on the mononuclear iridium ion coordinated with four nitrogen atom sites.

Introduction

Proton-exchange membrane fuel cells (PEMFCs) have been promoted as an ideal clean energy conversion system to alleviate dependence on fossil fuels and enable a sustainable energy future.^[1] However, the lack of low-cost and durable electrocatalysts to efficiently facilitate the sluggish oxygen reduction reaction (ORR) at the cathode remains as the weak point of this technology and severely obstructs its widespread implementation.^[2] In this context, single-atom catalysts

(SACs) have emerged as a highly promising category as they fulfill an ultimate metal utilization with excellent intrinsic activity when the catalytically active site can be well constructed.^[3] These unique characteristics endow SACs with potentially superior catalytic activity, and cost effectiveness and clarified catalytic mechanism when compared with the current mainstream research of Pt-based catalysts, macrocycle compounds and pyrolyzed M-N_x/C (M = Fe, Co) catalysts. Furthermore, by designing SACs which feature single organometallic centres, a bridge between homogeneous and heterogeneous catalysis can effectively be established to achieve concurrently high catalytic activity and durability.^[4] Given this, a variety of SACs configured with M-N-C (M = Fe, Co, Cu, Mn and Pt) sites have been explored for ORR catalysis with operational M-N₄ sites mimicking the biological porphyrin site in homogeneous catalysts.^[5] However, despite considerable progress achieved, the activities of these catalysts are still limited possibly due to the improper adsorption strengths to ORR intermediates,^[6] which calls for rational regulation of the d-electron structure of metal centres by well-selected metal atoms and coordinated ligands.

Following this trail, the adsorption free energy of OH* (ΔG_{OH^*}), a well-recognized reactivity descriptor for ORR, was calculated on a series of M-N-C SACs to determine an ideal metal centre. Among the various specimens, the atomic Ir-N-C configuration exhibits the nearest ΔG_{OH^*} to the apex of the classic Volcano plot^[7] (Figure S1). This is consistent with the fact that iridium porphyrins deliver the highest ORR activity in acidic electrolyte among other metal porphyrins,^[8] implying the superior activity of Ir-N-C for ORR catalysis.

[*] Dr. M. Xiao,^[†] Dr. H. Jin, Prof. S. Wang
College of Chemistry and Materials Engineering, Institute of New Materials and Industrial Technologies, Wenzhou University
Wenzhou, Zhejiang, 325035 (China)
E-Mail: Shunwang@wzu.edu.cn

N. Li, Dr. S. Li, Prof. D. Su
Centre for Functional Nanomaterials, Brookhaven National Laboratory, Upton, NY (USA)
E-Mail: dsu@bnl.gov

Dr. L. Ma, Dr. T. Wu
X-Ray Science Division, Argonne National Laboratory
Lemont, IL 60439 (USA)
E-Mail: twu@anl.gov

Dr. P. Cui
Key Laboratory of Soil Environment and Pollution Remediation, Institute of Soil Science, Chinese Academy of Sciences
Nanjing 210008 (P. R. China)

Dr. J. Lu
Chemical Sciences and Engineering Division, Argonne National Laboratory, Lemont, IL 60439 (USA)

Dr. M. Xiao,^[†] Dr. J. Zhu,^[†] Dr. G. Li, Z. P. Cano, P. Xu, Dr. G. Jiang, Prof. A. Yu, Prof. Z. Chen
Department of Chemical Engineering, University of Waterloo
Waterloo, Ontario (Canada)
E-Mail: zhwen@uwaterloo.ca

[†] These authors contributed equally to this work.

Supporting information and the ORCID identification number(s) for the author(s) of this article can be found under <https://doi.org/10.1002/anie.201905241>.

Motivated by this predictive basis, we synthesized, for the first time, a heterogenous iridium single-atom catalyst (Ir-SAC) towards high-efficiency ORR catalysis. The as-developed Ir-SAC displays a record-high turnover frequency (TOF) of $24.3 \text{ e}^- \text{ site}^{-1} \text{ s}^{-1}$ at 0.85 V vs. RHE, which outperforms all previously reported SACs and the commercial Pt/C benchmark. Remarkably, Ir-SAC also exhibits orders of magnitude enhancement in ORR activity when compared with metallic Ir nanoparticles. Density Functional Theory (DFT) calculations confirmed that the unique electronic structure of the Ir atom centre induced by the Ir-N₄ configuration contributes to an optimal adsorption energy that facilitates both the adsorption and desorption of ORR intermediates, thus leading to the unprecedented catalytic performance. This work not only offers an efficient and commercially competitive ORR catalyst, but also enlightens the fundamental understanding of the underlying structure–activity relationship, thus advancing valuable scientific and industrial developments for ORR catalysis.

Results and Discussion

Ir-SAC was synthesized using zeolite imidazolate frameworks-8 (ZIF-8, cavity diameter of 11.6 \AA)^[9] as active site host and the in situ encapsulated Ir acetylacetonate (molecular diameter of ca. 9.8 \AA) as guest, respectively, as illustrated in Figure 1 a. Our choice of Ir-impregnated ZIF-8 (Ir-ZIF-8) as the precursor was attributed to its prepotent environment, including the strong metal anchoring ability of N atoms and the space-confinement effect of micropores allowing the formation of SACs. Additionally, the as-derived highly porous

host architecture (Figure S2, S3 and Table S1) also guarantees the accessibility of the active metal centres to ORR reactions for maximum catalyst utilization. The well-maintained crystalline texture and the structural homogeneity of the as-prepared Ir-ZIF-8 were confirmed by X-ray diffraction (XRD) patterns (Figure S4) and scanning electron microscopy (SEM) with elemental mappings (Figure S5). This precursor was then subjected to heat-treatment under an H₂/Ar atmosphere to yield the final black Ir-SAC power (Digital images in Figure S6), as verified by the disappearance of sharp diffraction peaks for pristine Ir-ZIF-8 and the appearance of typical carbon peaks in the XRD patterns (Figure S7). Notably, the absence of diffraction peaks for crystalline Ir in the pyrolysis product implies the atomic Ir incorporation within the nitrogenous carbon skeleton.

The morphology and nanostructure of the obtained Ir-SAC were carefully examined by SEM and high angle annular dark-field scanning transmission electron microscope (HAADF-STEM) as shown in Figure 1 b and Figure S8, S9. The results clearly reveal the well-retained rhombododecahedron nanostructure and more importantly the absence of any observable Ir nanoparticles/nanoclusters. Nevertheless, the energy-dispersive spectrum elemental mappings (Figure 1 c–f) and Inductively Coupled Plasma (ICP) results evidently confirm the existence of iridium in the obtained Ir-SAC, suggesting an atomic-level Ir embedment within the carbon matrix. On this basis, aberration-corrected HAADF-STEM was further utilized for a direct discernment of the Ir distribution. The result displays plenty of speckled bright dots in the high-resolution HAADF-STEM image (Figure 1 g), which strongly confirms the atomic isolation of Ir in the obtained Ir-SAC. For comparative study, control samples with Ir supported on ZIF-8 derived nitrogenous carbon (N-C) and nitrogen-free carbon substrate (denoted as Ir/N-C and Ir/C, respectively) were also prepared (see details in Supporting Information). Both individual Ir atoms and Ir nanoparticles can be observed in Ir/N-C and Ir/C samples with a relatively lower density of Ir single atoms in the latter (Figure S10, S11), indicating that both the micropore structure and N doping are capable of anchoring the single Ir atoms effectively and preventing their aggregation. By contrast, the commercial Ir/C (denoted as Ir/C-Com) sample carries purely Ir nanoparticles with sizes of 2–4 nm as depicted in Figure S12.

Further evidence for the atomic dispersion of Ir in Ir-SAC as well as identification of the atomic coordination environment were demonstrated by extended X-ray absorption fine structure (EXAFS) and X-ray absorption near edge structure (XANES) spectroscopy (Figure 2 a, b). Commercial IrO₂ and Ir/C-Com catalysts were employed as benchmarks. In the Fourier transforms (FTs, R-space, Figure 2 a) for EXAFS, both Ir-SAC and IrO₂ show a single prominent peak located at ca. 1.5 \AA ascribed to the Ir-N/O scattering path, while Ir/C-Com shows a dominating peak at 2.3 \AA referring to the Ir-Ir scattering path. The absence of Ir-Ir scattering in the Ir-SAC spectrum strongly confirms its atomic isolation. By contrast, these two peaks can be clearly observed in the spectra of the Ir/N-C and Ir/C samples (Figure S13), indicating the coexistence of single-atom and nanoparticle-based Ir. Apart from that, EXAFS wavelet transform (WT)

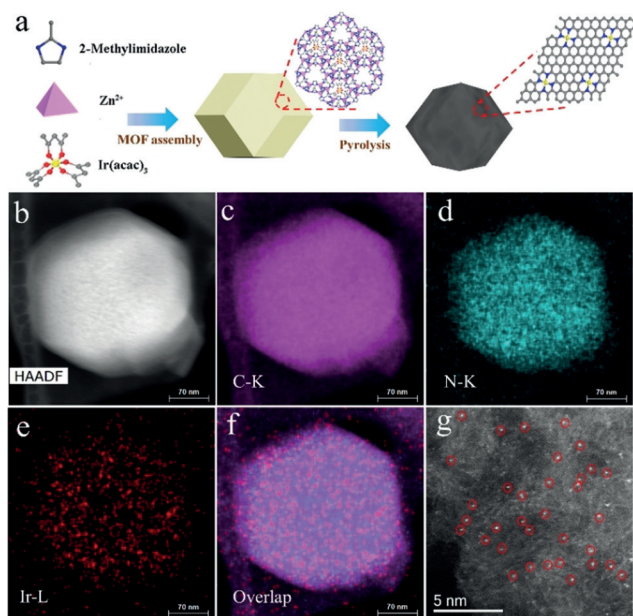


Figure 1. a) Scheme showing host–guest strategy for the fabrication of single atomic site catalysts; b–f) STEM images and the corresponding elemental mappings for the Ir-SAC; g) High-resolution HAADF-STEM image of Ir-SAC, with the distinct bright dots (circled in red) indicating Ir is atomically dispersed on the nitrogen doped carbon matrix.

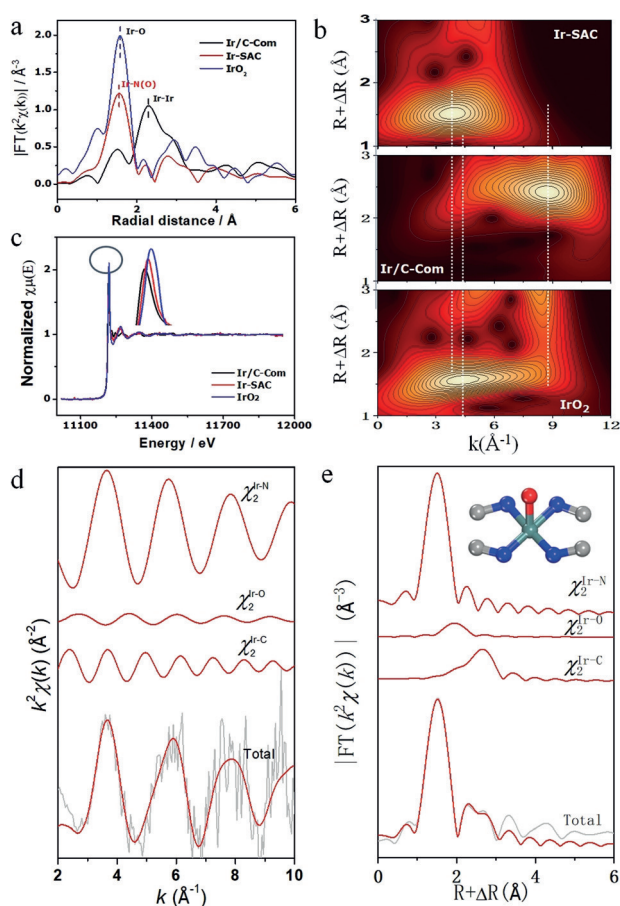


Figure 2. a) Fourier transforms of k^3 -weighted Ir L3-edge EXAFS data; b) Wavelet transforms for the k^3 -weighted Ir L3-edge EXAFS signals of Ir-SAC, Ir/C-Com and IrO₂; c) XANES of Ir L3-edge, where the white line intensity shows the valence state of Ir in Ir-SAC is between 0 and 4⁺; d,e) Ir L3-edge EXAFS of Ir-SAC in k (d) and R (e) spaces, where curves from top to bottom are the Ir-N, Ir-O and Ir-C two-body backscattering signals (χ_2) included in the fit and the total signal (red line) is superimposed on the experimental signal (black line). The measured and calculated spectra show excellent agreement.

analysis was performed for further confirmation of the atomic Ir dispersion, due to its capability of discriminating the backscattering atoms by providing not only radial distance resolution but also k -space resolution.^[10] In line with the FTs, the WT analysis of Ir-SAC reveals only one intensity maximum at approximately 3.8 \AA^{-1} (Figure 2b), which is assigned to the M-N contributions and suggests the complete absence of crystalline metal structures. In comparison, an intensity maximum at a higher k -space of 4.3 \AA^{-1} occurs in IrO₂, attributable to the Ir-O path, while a more positive shift of the intensity maximum to 7.7 \AA^{-1} can be observed for Ir/C-Com due to the Ir-Ir contribution. The coordination configuration in Ir-SAC was further investigated by quantitative least-squares EXAFS curve-fitting analysis using three backscattering paths: Ir-N, Ir-O and Ir-C (Figure 2d, e and Table S2). The best-fitting analysis shows clearly that the main peak at 1.5 \AA originates from Ir-N and Ir-O first-shell coordination with a coordination number of 4.2 and 0.8, respectively, whereas the minor satellite peak at 2.01 \AA is sa-

tisfactorily interpreted as the Ir-C contribution, suggesting a square-pyramidal configuration for the Ir-N/O bonding (inset in Figure 2e).

This unique configuration of single-atom Ir would contribute to a distinct electronic structure that differs from both the metallic Ir and Ir oxides, which in turn influences the adsorption behavior of the reaction intermediates and thereby affects the catalytic performance. Taking this into account, the electronic structure of the as-developed Ir-SAC was further examined by XANES and X-ray photoelectron spectroscopy (XPS). The XANES spectra demonstrates that the white-line intensity of Ir-SAC is located between those of Ir and IrO₂, indicating the partial oxidation of Ir in the form of Ir ^{δ +} (Figure 2c). Further valence state information was collected by XPS analysis (Figure S14), which revealed pure Ir³⁺ species in Ir-SAC, resembling the valence state of Ir in homogeneous iridium porphyrins.^[11] In contrast, both Ir³⁺ and Ir⁰ species were present in the Ir/N-C, and Ir/C samples, evidencing the copresence of single Ir atoms and metallic Ir clusters. These results strongly indicate the decreased electron density of Ir in the as-developed coordinative configuration, which is expected to weaken the intermediates' adsorption energy on Ir-SAC compared with its metallic crystalline counterpart and thereby improve ORR electrochemical kinetics by better facilitating the intermediate desorption.

In order to verify the potential electrochemical improvement, the ORR performance of the Ir-SAC was evaluated using the rotating disk electrode (RDE) and rotating ring-disk electrode (RRDE) techniques in 0.1M HClO₄ solution in comparison with Ir/N-C, Ir/C, Ir/C-Com and commercial Pt/C (Pt/C-TKK) catalysts. The catalyst surface was firstly activated by cyclic voltammetry (CV) in Ar-saturated 0.1M HClO₄ solution. The characteristic features of noble metal crystals in CV curve, hydrogen adsorption/desorption region and OH_{ads} layer region, diminish in the case of Ir-SAC, further reflecting the unmetallic nature of Ir-SAC (Figure 3a). Figure 3b shows the ORR polarization curves of different catalysts. Ir/C-Com exhibited the lowest ORR activity among the three Ir-based catalysts (Ir-SAC, Ir/N-C and Ir/C-Com), with onset (E_{onset}) and half-wave ($E_{1/2}$) potentials of 0.81 and 0.59 V, respectively. Benefiting from the additional Ir-N₄ moiety, the ORR activity of Ir/N-C was significantly increased with a 166 mV positive shift of the $E_{1/2}$. This enhancement likely originates from the participation of the isolated Ir-N₄ species, rather than those of the nitrogen-doped carbon (N-C) and/or the synergic effect between N-C and Ir nanoparticles, since both the pure N-C and Ir nanoparticles supported on N-C (Ir NPs/N-C) showed negligible ORR activity (Figure S15). By further regulating the Ir component to a pure single atom distribution, the as-developed Ir-SAC exhibited the highest catalytic performance as expected, featuring an ultra-high E_{onset} of 0.97 V and $E_{1/2}$ of 0.864 V, which outperforms most of the reported alternatives to platinum in acidic electrolyte (Table S3). It should also be noted that Ir/C, where single Ir atoms and Ir nanoparticles coexist, shows inferior ORR activity not only to the developed Ir-SAC but also to Ir/C-Com. This manifests the crucial roles of the synergism between downsizing the metal unit and the coordination environment in pursuit of high catalytic activity.

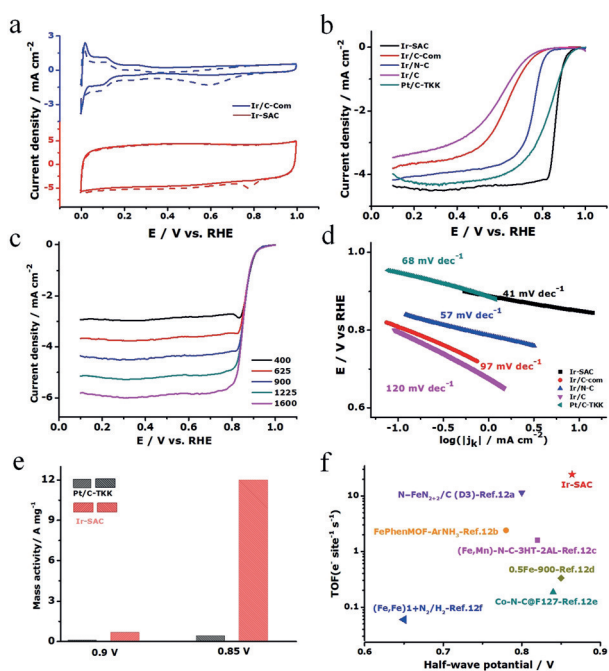


Figure 3. a) Cyclic voltammograms with a scanning rate of 50 mV s^{-1} in 0.1 M HClO_4 solution; b) ORR polarization curves with a scanning rate of 5 mV s^{-1} at rotating speed of 900 rpm for the synthesized catalysts; c) Tafel slopes for these catalysts; d) LSV curves of Ir-SAC with various rotation rates; e) Mass activity comparison between Ir-SAC and Pt/C-TTK; f) TOF and $E_{1/2}$ values of Ir-SAC and other recently reported SACs, where the TOF values were estimated at the potential of 0.85 V for Ir-SAC and 0.8 V for the other catalysts.

More interesting is that the Ir-SAC demonstrated even higher ORR activity than Pt/C as demonstrated by its more positive $E_{1/2}$. Considering the much lower metal loading on the electrode ($0.8 \text{ ug}_{\text{Ir}} \text{ cm}^{-2}$ vs. $6 \text{ ug}_{\text{Pt}} \text{ cm}^{-2}$), the as-developed Ir-SAC holds great promise for practical application by showing a much higher mass activity of $12.2 \text{ A mg}^{-1}_{\text{Ir}}$ at 0.85 V , corresponding to an exceptional 27-fold enhancement over Pt/C ($0.423 \text{ A mg}^{-1}_{\text{Pt}}$). It should be noted that the $E_{1/2}$ of Pt/C here is about 0.82 V due to the low loading of Pt on the electrode (Figure S16). Figure 3c shows Tafel slopes of 41 and 68 mV dec^{-1} for Ir-SAC and Pt/C, respectively, illustrating the faster ORR kinetics on Ir-SAC. Furthermore, the turnover frequency (TOF) was calculated to compare the intrinsic activity per active site to other notable catalysts. Intriguingly, Ir-SAC exhibited a record-high TOF of $24.3 \text{ e}^{-} \text{ site}^{-1} \text{ s}^{-1}$ (0.85 V vs. RHE), which is 5.6 times higher than that of commercial Pt/C ($3.63 \text{ e}^{-} \text{ site}^{-1} \text{ s}^{-1}$) and also the highest among Pt-free ORR catalysts,^[12] with the previously highest TOF reported as ca. $11.3 \text{ e}^{-} \text{ site}^{-1} \text{ s}^{-1}$ (0.80 V vs. RHE) on the D3 site^[12a] (Figure 3 f).

Apart from catalytic activity, the catalytic selectivity of the as-developed Ir-SAC towards ORR is also important to assess and was studied by Koutecky Levich (K-L) plots and the RRDE method. A four-electron pathway is found to dominate the ORR as deduced from K-L plots (Figure 3d and Figure S17). RRDE results also show the direct ORR pathway with a H_2O_2 yield as low as 3.5% (Figure S18).

As it known to all, single atom Pt catalysts have long been criticized by their high H_2O_2 yield due to the preferential end-on adsorption of oxygen molecules. In our case, the ultralow H_2O_2 of 3.5% strongly verified the realization of a nearly ideal four-electron ORR pathway on the Ir-SAC with a high energy conversion efficiency. This significant improvement is likely ascribed to the unique coordination environment of Ir that tailors the oxygen adsorption mode, which will be further studied in the following section.

As another important criterion of ORR catalysts, especially for SACs, the long-term operational stability of Ir-SAC was evaluated and compared with commercial Pt/C catalyst. A 20 mV negative shift of the $E_{1/2}$ can be observed for the Pt/C catalyst after 5000 cycles likely due to the Pt dissolution/aggregation and carbon support corrosion^[13] (Figure S19). By contrast, the Ir-SAC displays a much better stability by showing nearly undecayed ORR activity after 5000 continuous cycles (Figure S20). The high stability of Ir-SAC is attributed to the excellent anchoring effect of doped N to Ir atoms which effectively suppress Ir dissolution. In view of the high ORR activity and stability, the as-developed Ir-SAC was further employed in a H_2/O_2 fuel cell to investigate its catalytic ability in a practical energy conversion device (detailed methods in Supporting Information). A higher open circuit voltage of 0.955 V was achieved for the cell with the Ir-SAC-based cathode, which is comparable to that based on Pt/C (Figure S21). The maximum power density of the fuel cell reached 932 mW cm^{-2} , which is superior to most of the reported non-platinum ORR catalysts,^[14] further manifesting the great potential of Ir-SAC as a high-efficiency alternative to Pt-based catalysts in fuel cells.

Density functional theory (DFT) calculations were carried out to reveal the origins of the unprecedented electrocatalytic performance of Ir-SAC as well as the fundamental difference between the catalytic behaviors of a particle and a single atom. IrN_4 moiety doped in a graphene sheet (mimicking Ir-SAC), Ir_{19} cluster faceted with (111) faces on graphene and single Ir atom doped on pristine graphene (denoted as Ir-C-SAC) models were constructed (Figure S22). On the Ir-SAC site, O_2 molecule is preferentially adsorbed in the end-on model with an adsorption free energy ($\Delta G_{\text{O}_2^*}$) of -0.349 eV , whereas it adsorbs more strongly on Ir-C-SAC (-1.81 eV) and Ir_{19} cluster (-4.899 eV) in the side-on and bridge-*cis* model, respectively (Figure 4a, S23 and Table S4–6). The stronger adsorption energy would result in difficulty in desorption process, therefore leading to decreased ORR activity. This is verified by the ORR free energy diagrams of ORR on Ir-C-SAC and Ir_{19} cluster, where uphill energy profiles with OH^* desorption as rate-determining step at $U = 0$ were observed (Figure 4b, S24, 25). On the contrary, the free energy diagram of ORR on Ir-SAC exhibited a consistent downhill energy profile via an associative pathway with a limiting potential $U = 0.43 \text{ V}$ (Figure 4a, c) coinciding with its higher ORR activity. For an intuitive comparison, we further calculated the ORR overpotential on each catalytic site with the DFT model. A significantly lower overpotential was obtained on Ir-SAC (0.80 V) compared with those on the Ir-C-SAC (2.20 V) and the Ir_{19} cluster (1.64 V), indicating the much faster ORR kinetics on Ir-SAC. The activity sequence

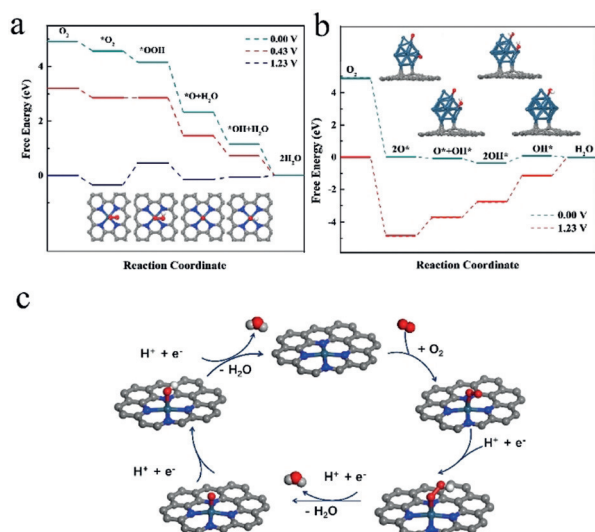


Figure 4. Gibbs free energy diagram for ORR on a) IrN₄, b) Ir₁₉ cluster; c) the proposed ORR mechanism on the IrN₄ site.

derived from DFT calculations implies the order of Ir/C (with co-existing Ir-C-SAC and Ir nanoparticles) < Ir/C-Com (only Ir nanoparticles) < Ir-SAC, which is in good consistency with the electrochemical results. It is also worth noting that this overpotential obtained by Ir-SAC is even comparable to that on bulk Pt (111),^[15] further manifesting the exceptional activity of Ir-SAC.

The above results have revealed that a moderate adsorption energy of ORR intermediates (especially OH (ΔG_{OH^*}), which was estimated to be located around the peak of the reported volcano plot of ORR activity in dependence of ΔG_{OH^*} ^[7]) on the developed Ir-SAC was responsible for its outstanding catalytic activity. The adsorption behaviour of intermediates on the catalyst was substantially determined by the electronic structure of the metal site, i.e., Ir in our case. Downsizing nanoparticles into single atoms alters the coordination environment of the metal atom and thus affects electronic structure dramatically. The charge density difference diagram of IrN₄ clearly shows the electron transfer from Ir atoms to the nearby N atoms, which turns the originally electroneutral Ir into positively charged and significantly different from the metallic state in the Ir₁₉ cluster (Figure 5 a, b). As the d-band centre is highly correlated with the metal-adsorbate interaction, the density of states (DOS) was calculated and estimated to be -2.89 eV and -2.65 eV for Ir-SAC and Ir₁₉ cluster, respectively (Figure 5 c,d and Figure S26 and Table S7). The downshifted d-band centre leads to a decreased adsorption energy consistent with the decreased ΔG_{OH^*} . The greater electron delocalization on the Ir₁₉ cluster contributed to its stronger adsorption ability to OH, which was confirmed by the DOS overlap of Ir 5d and O 2p in Figure 5 f. As for Ir-SAC, coordinated N atoms localized the d-electrons of Ir and therefore decreased its adsorption energy to OH.

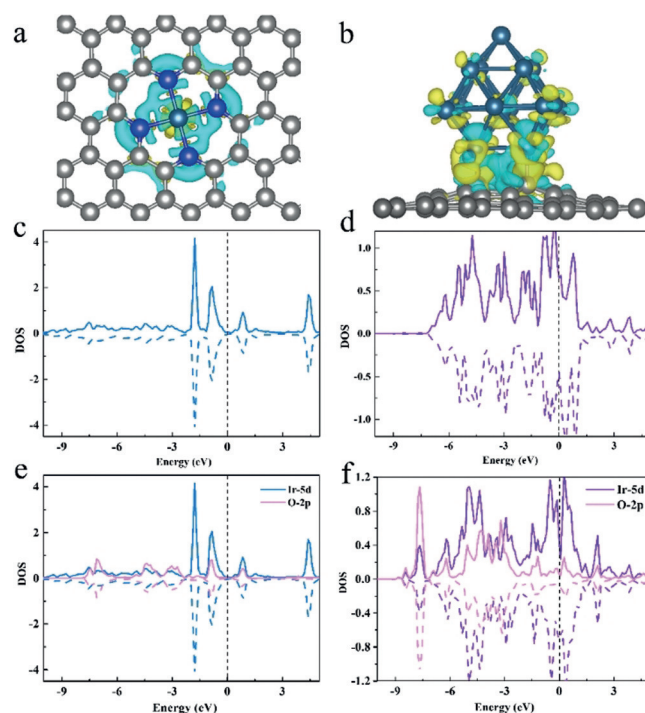


Figure 5. Charge density difference for a) IrN₄ and b) Ir₁₉ cluster on graphene; the calculated pDOS of Ir site for c) IrN₄ and d) Ir₁₉ cluster on graphene; the calculated pDOS of Ir site and O 2p for e) IrN₄ and f) Ir₁₉ cluster on graphene with adsorbed OH*.

Conclusions

We developed an Ir-N-C single atom catalyst to mimic homogeneous iridium catalysts for ORR in acidic electrolyte. The obtained Ir-SAC demonstrated an exceptionally high ORR activity with mass activity of 12.2 A g^{-1} , which is significantly higher than both commercial Pt/C and Ir/C. Moreover, the Ir-SAC achieved a record-high TOF of $24.3 \text{ e}^- \text{ site}^{-1} \text{ s}^{-1}$ among all the previously-reported SACs. The active site was determined to be the mononuclear Ir coordinated with four N atoms by TEM and XAS analysis, while the fundamental reason of the unprecedented catalytic activity was attributed to the moderate adsorption energy of the ORR intermediates on Ir-SAC as revealed by DFT calculation. The findings in this work offer an in-depth understanding as well as important guidance for future development of high-performance SACs.

Acknowledgements

We thank the University of Waterloo and Wenzhou University for financial support and The Catalysis Research for Polymer Electrolyte Fuel Cells (CaRPE FC) Network administered from Simon Fraser University and supported by Automotive Partnership Canada (APC) Grant no. APCPJ 417858-11 through the Natural Sciences and Engineering Research Council of Canada (NSERC). H.L.J. and S.W. are grateful for financial support from the National Natural Science Foundation of China (51872209 and 51772219) and

the Zhejiang Provincial Natural Science Foundation of China (LZ17E02002). Electron microscopy work was performed at the Center for Functional Nanomaterials, Brookhaven National Laboratory, which is supported by the U.S. Department of Energy (DOE), Office of Basic Energy Science, under Contract No. DE-SC0012704. Research conducted at beamline 9-BM used resources of the Advanced Photon Source, an Office of Science User Facility operated for the U.S. Department of Energy (DOE) Office of Science by Argonne National Laboratory under Contract No. DE-AC02-06CH11357. J.L. gratefully acknowledges support from the U.S. Department of Energy (DOE), Office of Energy Efficiency and Renewable Energy, Vehicle Technologies Office. Argonne National Laboratory is operated for DOE Office of Science by UChicago Argonne, LLC, under contract number DE-AC02-06CH11357.

Conflict of interest

The authors declare no conflict of interest.

Stichwörter: Adsorptionsenergie · Brennstoffzellen · Einzelatomkatalysator · Iridium · Sauerstoffreduktionsreaktion

Zitierweise: *Angew. Chem. Int. Ed.* **2019**, *58*, 9640–9645
Angew. Chem. **2019**, *131*, 9742–9747

- [1] a) V. Mehta, J. S. Cooper, *J. Power Sources* **2003**, *114*, 32–53; b) H. A. Gasteiger, N. M. Markovic, *Science* **2009**, *324*, 48–49.
- [2] a) M. D. Allendorf, *Nat. Energy* **2016**, *1*, 16058; b) C. Yang, H. Jin, C. Cui, J. Li, J. Wang, K. Amine, J. Lu, S. Wang, *Nano Energy* **2018**, *54*, 192–199.
- [3] a) B. T. Qiao, A. Q. Wang, X. F. Yang, L. F. Allard, Z. Jiang, Y. T. Cui, J. Y. Liu, J. Li, T. Zhang, *Nat. Chem.* **2011**, *3*, 634–641; b) X. F. Yang, A. Q. Wang, B. T. Qiao, J. Li, J. Y. Liu, T. Zhang, *Acc. Chem. Res.* **2013**, *46*, 1740–1748; c) C. Z. Zhu, S. F. Fu, Q. R. Shi, D. Du, Y. H. Lin, *Angew. Chem. Int. Ed.* **2017**, *56*, 13944–13960; *Angew. Chem.* **2017**, *129*, 14132–14148; d) Y. Chen, S. Ji, C. Chen, Q. Peng, D. Wang, Y. Li, *Joule* **2018**, *2*, 1242–1264; e) H. Zhang, G. Liu, L. Shi, J. Ye, *Adv. Energy Mater.* **2018**, *8*, 1701343.
- [4] a) X. Cui, W. Li, P. Ryabchuk, K. Junge, M. Beller, *Nat. Catal.* **2018**, *1*, 385–397; b) A. Wang, J. Li, T. Zhang, *Nat. Rev. Chem.* **2018**, *2*, 65–81.
- [5] a) C. Z. Zhu, Q. R. Shi, B. Z. Xu, S. F. Fu, G. Wan, C. Yang, S. Y. Yao, J. H. Song, H. Zhou, D. Du, S. P. Beckman, D. Su, Y. H. Lin, *Adv. Energy Mater.* **2018**, *8*, 1801956; b) H. X. Xu, D. J. Cheng, D. P. Cao, X. C. Zeng, *Nat. Catal.* **2018**, *1*, 339–348; c) S. Yang, J. Kim, Y. J. Tak, A. Soon, H. Lee, *Angew. Chem. Int. Ed.* **2016**, *55*, 2058–2062; *Angew. Chem.* **2016**, *128*, 2098–2102; d) X. X. Wang, D. A. Cullen, Y. T. Pan, S. Hwang, M. Y. Wang, Z. X. Feng, J. Y. Wang, M. H. Engelhard, H. G. Zhang, Y. H. He, Y. Y. Shao, D. Su, K. L. More, J. S. Spendelow, G. Wu, *Adv. Mater.* **2018**, *30*, 1706758; e) Y. J. Chen, S. F. Ji, Y. G. Wang, J. C. Dong, W. X. Chen, Z. Li, R. A. Shen, L. R. Zheng, Z. B. Zhuang, D. S. Wang, Y. D. Li, *Angew. Chem. Int. Ed.* **2017**, *56*, 6937–6941; *Angew. Chem.* **2017**, *129*, 7041–7045; f) J. Li, M. Chen, D. A. Cullen, S. Hwang, M. Wang, B. Li, K. Liu, S. Karakalos, M. Lucero, H. Zhang, C. Lei, H. Xu, G. E. Sterbinsky, Z. Feng, D. Su, K. L. More, G. Wang, Z. Wang, G. Wu, *Nat. Catal.* **2018**, *1*, 935–945; g) H. H. Wu, H. B. Li, X. F. Zhao, Q. F. Liu, J. Wang, J. P. Xiao, S. H. Xie, R. Si, F. Yang, S. Miao, X. G. Guo, G. X. Wang, X. H. Bao, *Energy Environ. Sci.* **2016**, *9*, 3736–3745; h) T. Okada, M. Gokita, M. Yuasa, I. Sekine, *J. Electrochem. Soc.* **1998**, *145*, 815–822; i) S. L. Gojković, S. Gupta, R. F. Savinell, *J. Electrochem. Soc.* **1998**, *145*, 3493–3499; j) R. Jasinski, *Nature* **1964**, *201*, 1212.
- [6] H. Xu, D. Cheng, D. Cao, X. C. Zeng, *Nat. Catal.* **2018**, *1*, 339–348.
- [7] F. Calle-Vallejo, J. I. Martinez, J. Rossmeisl, *Phys. Chem. Chem. Phys.* **2011**, *13*, 15639–15643.
- [8] J. A. R. van Veen, J. F. van Baar, C. J. Kroese, J. G. F. Coolegem, N. Dewit, H. A. Colijn, *Ber. Bunsen-Ges.* **1981**, *85*, 693–700.
- [9] M. Xiao, J. Zhu, L. Ma, Z. Jin, J. Ge, X. Deng, Y. Hou, Q. He, J. Li, Q. Jia, S. Mukerjee, R. Yang, Z. Jiang, D. Su, C. Liu, W. Xing, *ACS Catal.* **2018**, *8*, 2824–2832.
- [10] H. Funke, A. C. Scheinost, M. Chukalina, *Phys. Rev. B* **2005**, *71*, 094110.
- [11] H. Cui, Y. Wang, Y. Wang, Y.-Z. Fan, L. Zhang, C.-Y. Su, *Cry-EngComm* **2016**, *18*, 2203–2209.
- [12] a) U. I. Kramm, J. Herranz, N. Larouche, T. M. Arruda, M. Lefèvre, F. Jaouen, P. Bogdanoff, S. Fiechter, I. Abs-Wurmbach, S. Mukerjee, J.-P. Dodelet, *Phys. Chem. Chem. Phys.* **2012**, *14*, 11673–11688; b) J. Li, S. Ghoshal, W. Liang, M.-T. Sougrati, F. Jaouen, B. Halevi, S. McKinney, G. McCool, C. Ma, X. Yuan, Z.-F. Ma, S. Mukerjee, Q. Jia, *Energy Environ. Sci.* **2016**, *9*, 2418–2432; c) N. R. Sahraie, U. I. Kramm, J. Steinberg, Y. Zhang, A. Thomas, T. Reier, J.-P. Paraknowitsch, P. Strasser, *Nat. Commun.* **2015**, *6*, 8618; d) A. Zitolo, V. Goellner, V. Armel, M.-T. Sougrati, T. Mineva, L. Stievano, E. Fonda, F. Jaouen, *Nat. Mater.* **2015**, *14*, 937; e) Y. He, S. Hwang, D. A. Cullen, M. A. Uddin, L. Langhorst, B. Li, S. Karakalos, A. J. Kropf, E. C. Wegener, J. Sokolowski, M. Chen, D. Myers, D. Su, K. L. More, G. Wang, S. Litster, G. Wu, *Energy Environ. Sci.* **2019**, *12*, 250–260; f) U. I. Kramm, I. Herrmann-Geppert, J. Behrends, K. Lips, S. Fiechter, P. Bogdanoff, *J. Am. Chem. Soc.* **2016**, *138*, 635–640.
- [13] a) X. Yu, S. Ye, *J. Power Sources* **2007**, *172*, 145–154; b) S. Sun, G. Zhang, D. Geng, Y. Chen, R. Li, M. Cai, X. Sun, *Angew. Chem. Int. Ed.* **2011**, *50*, 422–426; *Angew. Chem.* **2011**, *123*, 442–446; c) S. D. Knights, K. M. Colbow, J. St-Pierre, D. P. Wilkinson, *J. Power Sources* **2004**, *127*, 127–134.
- [14] a) M. Lefèvre, E. Proietti, F. Jaouen, J. P. Dodelet, *Science* **2009**, *324*, 71–74; b) G. Wu, K. L. More, C. M. Johnston, P. Zelenay, *Science* **2011**, *332*, 443–447; c) K. Strickland, M. W. Elise, Q. Y. Jia, U. Tylus, N. Ramaswamy, W. T. Liang, M. T. Sougrati, F. Jaouen, S. Mukerjee, *Nat. Commun.* **2015**, *6*, 7343; d) E. Proietti, F. Jaouen, M. Lefevre, N. Larouche, J. Tian, J. Herranz, J. P. Dodelet, *Nat. Commun.* **2011**, *2*, 416.
- [15] a) J. K. Nørskov, J. Rossmeisl, A. Logadottir, L. Lindqvist, J. R. Kitchin, T. Bligaard, H. Jónsson, *J. Phys. Chem. B* **2004**, *108*, 17886–17892; b) D. H. Lim, J. Wilcox, *J. Phys. Chem. C* **2012**, *116*, 3653–3660.

Manuskript erhalten: 27. April 2019
Akzeptierte Fassung online: 23. Mai 2019
Endgültige Fassung online: 18. Juni 2019